Extreme Mechanics Letters 5 (2015) 74–80

Contents lists available at ScienceDirect

Extreme Mechanics Letters

journal homepage: www.elsevier.com/locate/eml

Pressure and shear-induced amorphization of silicon

S. Zhao [a], B. Kad [a], E.N. Hahn [a], B.A. Remington [c], C.E. Wehrenberg [c], C.M. Huntington [c], H.-S. Park [c], E.M. Bringa [b,d], K.L. More [e], M.A. Meyers [a,*]

[a] University of California, San Diego, La Jolla, CA 92093, USA
[b] Facultad de Ciencias Exactas y Naturales, UNCuyo, Mendoza 5500, Argentina
[c] Lawrence Livermore National Laboratory, Livermore, CA 94550, USA
[d] CONICET, Mendoza 5500, Argentina
[e] Oak Ridge National Laboratory, Oak Ridge, TN 37831, USA

ARTICLE INFO

Article history:
Received 31 August 2015
Accepted 1 October 2015
Available online 22 October 2015

Keywords:
Laser shock compression
Silicon
Amorphization
Nanocrystalline Silicon

ABSTRACT

Here we report that high-power, pulsed, laser-driven shock compression of monocrystalline silicon produces directional amorphization, revealed by high-resolution transmission electron microscopy and confirmed by molecular dynamics simulations. At the lowest energy level experiment, generating a pressure of ∼4 GPa, silicon reacts elastically. At intermediate energy levels (P∼11 and 22 GPa), amorphization is observed both at the surface and directionally, along planes making angles close to the maximum shear. At the highest laser energy level explored here, (P_{peak} ∼28 GPa), the recovered sample shows a nanocrystalline microstructure near the surface. This nanocrystalline structure forms by crystallization from the amorphous phase and is thought to be a post-shock phenomenon. Shear-induced lattice defects (stacking faults and twins) on crystallographic slip planes play a crucial role in the onset of amorphization. Molecular dynamics show that silicon behaves elastically until ∼10 GPa and, at slightly higher pressures, partial dislocations and stacking faults are emitted from the surface. Driven by the high-amplitude stress pulse, these defects travel inwards along specific crystallographic orientations and intersect, leading to further defect creation, additional plastic work, and, at higher pressures, amorphous bands in intersecting patterns. The typical high-pressure solid–solid phase transitions of silicon are not observed whereas the high shear stresses are relaxed by localized dislocation motion/interactions and eventually by directional amorphization, which occurs below the critical hydrostatic pressure for melting of silicon in shock compression. It is therefore proposed that the combined effects of hydrostatic and shear stresses lead to directional amorphization.

1. Introduction

The importance of shear stresses in reactions and phase transitions can be significant and, in some cases, dominant [1–3]. During laser-shock compression, the coexistence of strong hydrostatic and deviatoric stresses often produces mechanical responses unique to the extreme stresses and timescales involved. Recently, Levitas and Ravelo [4] showed the role of fast, non-hydrostatic compression in generating "virtual melting" in metals subjected to high strain-rate loading. Amorphization is usually achieved by quenching liquid matter below its glassy transition temperature to hinder crystallization. For silicon, other processes such as plasma deposition [5], static pressure by diamond anvil cell [6], radiation damage [7], indentation [8], and impact by nanodroplets [9] have been used to produce amorphization that is either highly

* Corresponding author.
E-mail address: mameyers@eng.ucsd.edu (M.A. Meyers).

http://dx.doi.org/10.1016/j.eml.2015.10.001
2352-4316/

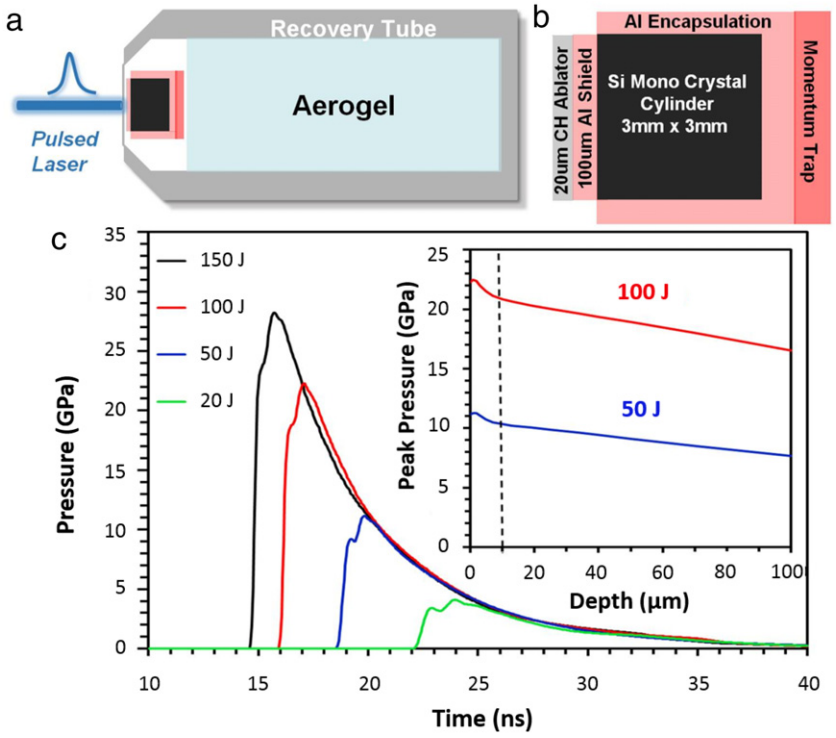

Fig. 1. Experimental setup using high-energy pulsed lasers to launch a short duration (∼few ns) blast wave through single crystal Si. (a) Overall experimental setup showing the target package and recovery tube. Si single crystal is [001] oriented and has dimensions of ⌀3 mm × 3 mm. (b) Magnification of the target package, showing a CH ablator (polystyrene) used to produce a plasma under laser irradiation, an Al heat shield that also tamps the Si sample from the front, an Al "encapsulation" to laterally confine the sample on the sides, and a rear Al momentum trap. (c) Calculated pressure–time plots at four energy levels corresponding to the four laser shock experiments. The *x* axis denotes time in ns, given from the shock traveling from the CH/Al interface. The inset illustrates the simulated shock pressure versus depth into the silicon sample relative to the Al/Si interface for the 50 and 100 J laser shots.

defective or severely localized. Recovery of amorphous silicon from high-pressure experiments has been an outstanding goal for decades [10]. Here we present successful recovery of laser-shocked silicon and identify bulk amorphization, in addition to directional amorphous bands penetrating into the sample. The mechanism of large scale directional amorphization has been predicted by Molecular Dynamics (MD) simulation of the Ni–Zr system [11], but never heretofore observed experimentally.

2. Experimental materials and methods

A schematic of the experiment can be seen in Fig. 1(a), with cylindrical single crystal silicon targets encapsulated in aluminum. The silicon was procured in the condition of 3 mm diameter cylinders with a 3 mm length with the top and bottom surfaces lapped. The aluminum capsules were heated and the cylinders inserted into them, to minimize the gap between specimen and capsule. Aluminum has a sonic impedance close to that of silicon and serves to minimize any tensile reflections, limiting fragmentation of the target. Laser experiments were conducted at Omega Laser Facility, Laboratory for Laser Energetics, University of Rochester. The sources are pulsed neodymium glass lasers, frequency tripled to give a 351 nm wavelength. Nominal laser energies for the experiment were 20, 50, 100, and 150 J, each with a full width half max pulse duration of 1 ns and nominally square pulse shape in time. No phase plate was used in order to broaden exposure to the laser over the entire specimens and lessen lateral pressure gradients. The laser spot size focused on the target package was approximately 3 mm in diameter. Radiation–hydrodynamic simulations were used to calculate the shock-wave propagation through the aluminum and into the silicon samples. The shock pressure profiles at the Al/Si interface are given in Fig. 1(c). The peak pressures should be taken as first-order reference values. Rigorous calculations were undertaken to produce these values, but given the uncertainties in the driven intensity, ablation pressure scaling, and variations across shot days, we estimate that the uncertainty in the shock pressure at the Al/Si interface is ±13%. The pressure calibration is described further in the supplementary materials section (Fig. S2). Nevertheless, the intricate target package allowed for successful recovery of shocked silicon crystals and the subsequent direct microstructural characterizations are of primary focus here.

3. Characterization of shock-recovered silicon

Characterization of the recovered silicon targets by transmission electron microscopy (TEM) and high resolution TEM (HRTEM) is shown in Fig. 2. Electron transparent thin foils were extracted from the approximate center of the as-shocked surface by focused ion beam (FIB) and full details are supplied within the supplementary materials section (Fig. S3). At the lowest laser energy, 20 J

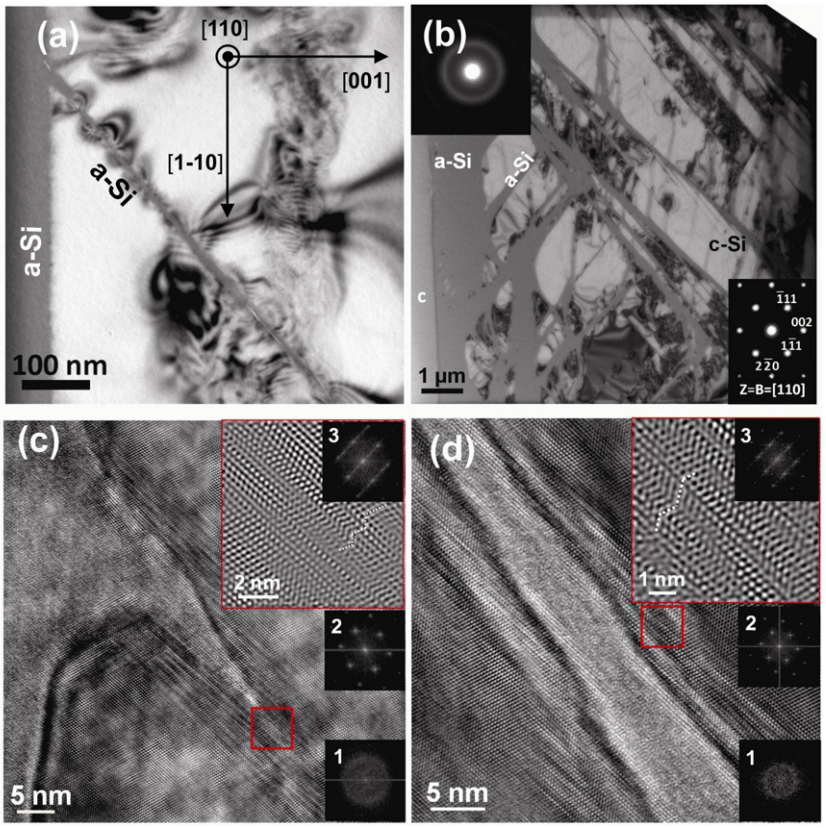

Fig. 2. Characterization of laser shock compressed [001] silicon single crystal (shock wave from left to right): (a) TEM micrograph of laser shock-recovered sample at 50 J, $P_{peak} = 4$ GPa, showing amorphous layer at surface, from which an amorphous band is emitted. (b) At 100 J, $P_{peak} = 11$ GPa, the recovered silicon sample shows much broader amorphous regions, marked "a-Si" with corresponding diffraction pattern on upper left inset; crystalline "islands" are marked by "c-Si" with diffraction pattern in lower right inset. The appearance of (002) spot is due to the strong double diffraction effect of {111} planes. (c) High resolution TEM micrograph indicating the shear-originated amorphous bands surrounded by stacking faults/micro (nano) twins. (d) High resolution TEM image at a deeper site of the sample showing that the amorphous band deviates away from {111} plane. (c) and (d) are taken from the same TEM sample as in (a) and (b), respectively, and the faulted regions are highlighted in red box with inverse FFT view in the upper right box. Three insets, marked 1, 2, 3, show the fast FFT diffraction patterns of amorphous, crystalline and heavily faulted regions, respectively. (For interpretation of the references to color in this figure legend, the reader is referred to the web version of this article.)

($P_{peak} \sim 4$ GPa), silicon exhibits purely elastic behavior, i.e., neither phase transitions, nor defects were observed, consistent with previous reports of elasticity at such pressures [12,13]. The significant difference observed between a reference unshocked specimen and the laser-shocked sample confirms that subsequent observations are not artifacts of sample preparation using focused ion beam. This comparison is provided in the supplementary materials section (Fig. S3).

At intermediate energy levels of 50 J ($P_{peak} \sim 11$ GPa) and 100 J ($P_{peak} \sim 22$ GPa), conventional bright field TEM shows that the laser-shocked region has both a bulk amorphous silicon layer adjacent to the surface and amorphous bands penetrating into the crystal. The amorphous material shows a characteristic featureless appearance, displaying a halo-shaped diffraction pattern, as shown in the upper left inset in Fig. 2(b), with an absence of spots or sharp rings. The amount of amorphous material increases as the laser energy rises from 50 J (Fig. 2(a)) to 100 J GPa (Fig. 2(b)), i.e. the surface layer becomes thicker (from 100 nm to 1 μm) and sub-surface bands broaden. The 'islands' of crystalline material isolated between the intersecting amorphous bands become smaller near the surface. The bands appear to be crystallographically aligned and multiple variants are to be expected, given the symmetry of the [001] crystal orientation. Numerous secondary feather-shaped bifurcations originating from the primary amorphous bands are observed in Fig. 2(b). This is also illustrated later in the molecular dynamics (MD) simulation (Fig. 3(b), (c)) as secondary {111} growth variants.

The high resolution TEM micrograph, Fig. 2(c), reveals what appears to be an early stage of the amorphous band's formation and penetration into the crystalline lattice, indicating that the bands initiate at {111} planes. Abundant {111} stacking faults and nano-twins are identified in the vicinity of the amorphous band, exhibiting zigzag configurations as seen in the red box and upper right inset. The faulted region shows extra twin spots and streaking normal to {111} reflections, consistent with the planar directionality of the stacking faults and/or nano-twins. The amorphous band shows an asymmetric growth: the top part of the band is aligned with {111} plane, whereas the bottom bounding surface is misaligned by approximately 10%. This can be explained by the angle of maximum

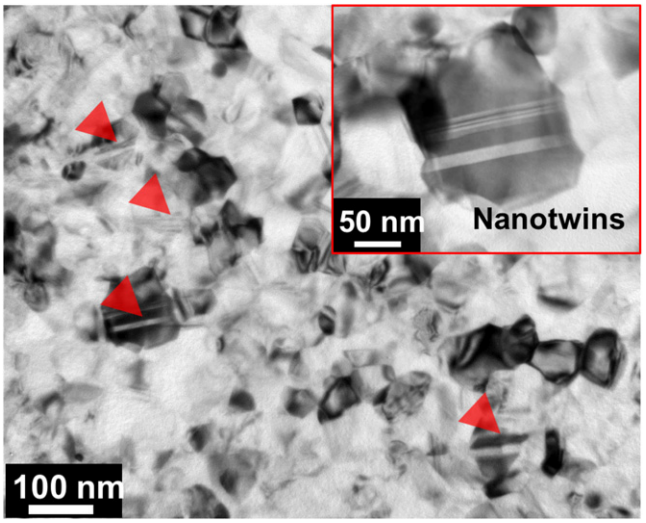

Fig. 3. Nanocrystals. TEM micrograph of 150 J shocked sample, showing nanocrystallization with massive nano-twinning observed.

shear which forms a cone in the specimen, whereas the slip planes are flat surfaces. Although the process initiates along slip planes, the bands reorient toward the direction of maximum shear stress as the amorphization evolves. The fast Fourier transformations (FFT) at the amorphous, bulk crystalline and heavily faulted regions adjacent to the amorphous bands are also given as inserts in Fig. 2(c) and (d). Fig. 2(d) shows a late-stage amorphous band at about 4 μm depth below the shock surface. In this particular case, the 5 nm thick band deviates approximately 10–15° from {111} planes, consistent with the previously observed misorientations seen in conventional TEM images, Fig. 2(a), (b).

At the highest laser energy explored here, 150 J ($P_{peak} \sim$ 28 GPa), the recovered sample shows a nanocrystalline microstructure near the surface. The grain size ranges from ∼100 nm to just several nm, decreasing with increasing distance from the energy deposition surface. Amorphous bands are preserved at depths greater than 10 μm below the shock surface. Notably, nanotwins with spacing of several to tens of nanometers can be observed in the newly formed grains, which have a size of approximately 100 nm in Fig. 3 but which increases toward the surface.

4. Molecular dynamics simulations

In order to elucidate the formation of directional amorphous bands, large-scale molecular dynamics simulations of Si were carried out using LAMMPS [14] under uniaxial shock compression using a frozen piston methodology [15]. There are many interatomic potentials used to describe Si under different conditions. We select a modified parameterization [16] of the Tersoff potential [17], which describes reasonably well crystalline, liquid, and amorphous silicon, including the kinetics of the crystal to liquid transition [18]. The empirical potential used here was not explicitly parameterized for accurate extrapolation of the elastic moduli with pressure (Supplementary Materials, Fig. S1), the Hugoniot (Supplementary Materials, Fig. S4), nor stacking fault energies (Fig. S5) and good agreement should be taken positively.

Molecular dynamics snapshots at two pressures, 12 and 16 GPa, are shown in Fig. 4. The sequence of events follows closely that of Fig. 2. The sample behaves elastically until ∼10 GPa and, at slightly higher pressures, partial dislocations and stacking faults are first emitted from the surface (light blue lines in Fig. 4(a)), consistent with a previous report that dislocations are more aptly to nucleate at the surface [20]. Driven by the high-amplitude stress pulse, these defects travel from the surface inwards along specific crystallographic orientations and intersect, leading to further defect creation and additional plastic work. At higher pressures, amorphous bands form in intersecting patterns. As mentioned earlier (Section 3), the amorphous bands originate from crystallographic slip planes and deviate toward the angle of maximum shear.

Simulations by Phillpot et al. [21,22] found that melting would typically initiate at surfaces or grain boundaries in Si. It is clear that defects may facilitate disordering and this is further supported by Gomez et al. [23], who found that dislocations mediated melting in a model solid. Snapshots given in Fig. 4(a), (b) represent the state of the material during loading and we would also like to directly compare our simulations with recovered TEM specimens. Fig. 4(c) shows a simulated recovery of Fig. 4(b) sample carried out over 50 ps. Details of this procedure are given in the Supplementary Materials Section (see Appendix A). A good deal of similar structural characteristics can be seen between the recovered and shock-loaded condition. The most evident microstructural difference is the retraction of unpinned stacking faults and a decrease in the coordination of the transformed amorphous material due to rapid quenching.

The relatively long time scale of the experiment might lead to structural changes which are thermally activated and which cannot be sampled by our MD simulations. However, given the tremendous agreement in spatial scales – comparing Fig. 2(c)–(d) and Fig. 4, where amorphous bands are only about 5 nm thick, with stacking

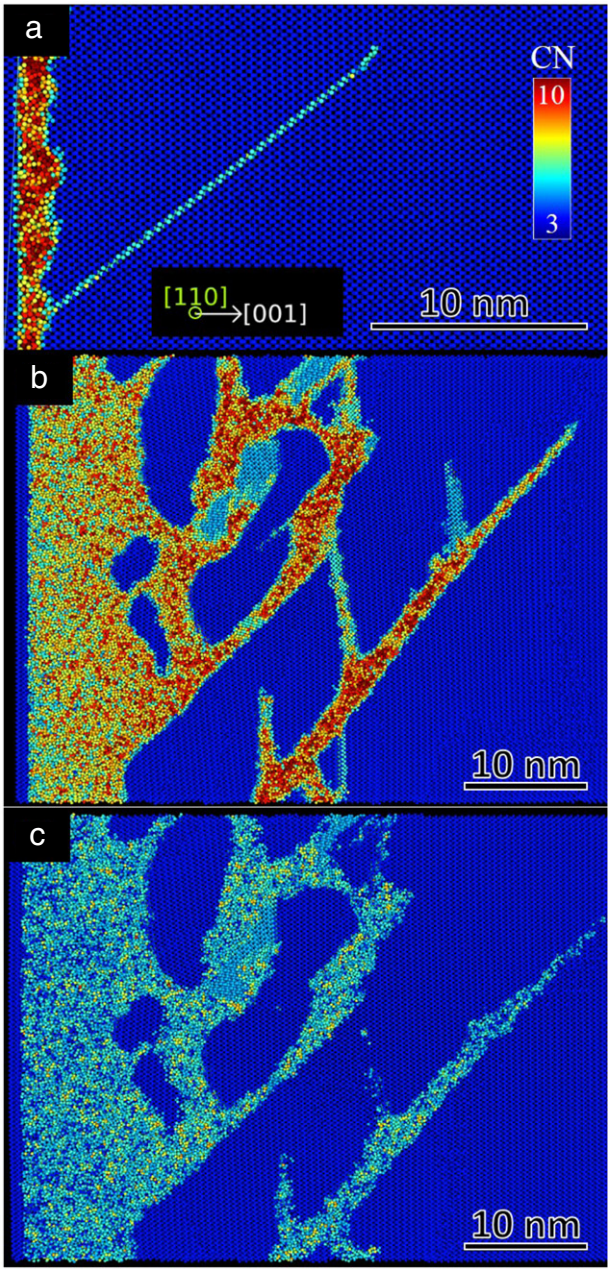

Fig. 4. Visualization of molecular dynamics simulations using OVITO [19]. Uniaxial impact loading of ⟨001⟩ single crystalline silicon. Atom color indicates coordination number as shown in (a). Snapshots were taken under various loading conditions: (a) 0.85 km/s, 12 GPa, and 25 ps, (b, c) 1.1 km/s, 16 GPa, 25 ps and simulated recovery at 75 ps respectively. Associated transitions from (a) stacking faults to (b) disordering along bands produced by shear strain. The microstructure of (b) after shock release and recovery is presented in (c) where unloading reduces unstable stacking faults and decreases the average coordination from 6.7 to 5.1 within the amorphous region. (For interpretation of the references to color in this figure legend, the reader is referred to the web version of this article.)

faults which are only 1 nm thick – and patterns between MD and the experiments, it seems possible that the crystalline-to-amorphous transition occurs within the same time frame observed in the simulations, and that the material is "locked" there, despite the possible occurrence of late thermally-activated events.

Fig. 5 details the increase in shock temperature and the attendant decrease in melting point for Si with increasing pressure; both molecular dynamics and analytical calculations are shown and place the critical pressure for melting between 12 and 17 GPa [6,10,27]. Earlier calculations based on experiments by Nesterenko [10] indicate a value of 11.5 GPa. The negative Clausius–Clapeyron slope ($\frac{dT_{melt}}{dP} < 0$) for silicon [28] is responsible for the decrease in melting point with hydrostatic pressure, whereas the majority of materials exhibit an increase with pressure. The experimentally observed directional amorphization occurs at a

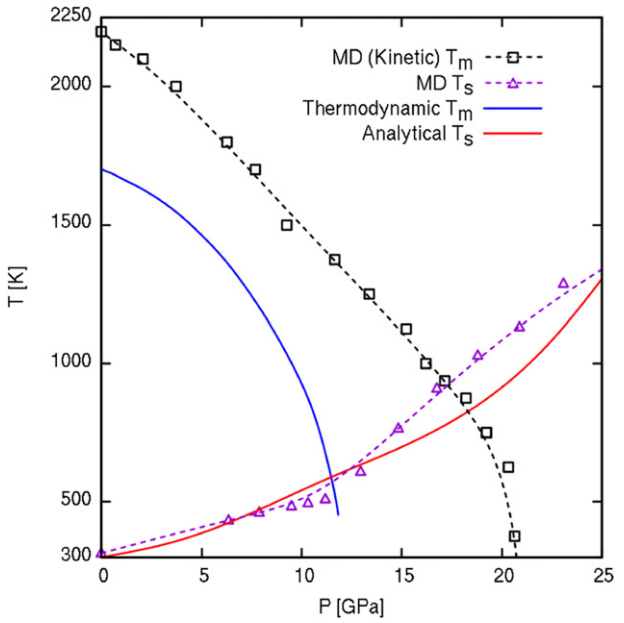

Fig. 5. Comparison of pressure dependence of shock-induced temperature rise and decrease of melting temperature. The temperature rise at the shock front can be determined analytically [24] (solid red line) as well as by MD simulation (dashed purple line and triangles). The detailed derivation of temperature rise is given in the Supplementary Materials Section [25] and the Rankine–Hugoniot relationship of silicon was adopted from reference [26]. The MD-predicted T_m vs. P (dashed black line and squares) is compared with the $T - P$ phase diagram (solid blue line) re-plotted from Ref. [7]. (For interpretation of the references to color in this figure legend, the reader is referred to the web version of this article.)

pressure (∼10 GPa, as shown in Fig. 1(c)) slightly lower than the "melting pressure" predicted above.

5. Shear stresses in shock compression

Laser shock creates a rapid uniaxial strain state with corresponding stresses that have hydrostatic and deviatoric (shear) components. For purely elastic uniaxial deformation:

$$\sigma_{ij} = C_{ijkl}\varepsilon_{kl} = C_{ij33}\varepsilon_{33} \tag{1}$$

where $i, j = 1, 2, 3$ and 3 represents the loading direction coincident with the [001] orientation of the crystal. Therefore, $\tau_{\max}$ is related to P by,

$$\frac{\tau_{\max}}{P} = \frac{3(C_{11} - C_{12})}{2(C_{11} + 2C_{12})}. \tag{2}$$

For silicon, the ambient elastic moduli, $C_{11} = 165.7$ GPa and $C_{12} = 63.9$ GPa [29], render $\frac{\tau_{\max}}{P} = 0.52$. This value is in agreement with molecular dynamics simulations of pressure-dependent C_{ij} and $\frac{\tau_{\max}}{P}$ (see Supplementary Materials, Fig. S1). Although the ratio decreases to 0.26 at 20 GPa, this value is still significant. Critically, hydrostatic pressure alone does not produce line defects in crystals of cubic symmetry (but can introduce them in anisotropic hexagonal polycrystals because of compatibility stresses), whereas shear stresses are responsible for plastic deformation and generation of lattice imperfections such as dislocations, stacking faults, and twinning. The point defect concentration, on the other hand, can be altered by both hydrostatic and deviatoric stresses.

6. Conclusions

In the lower amplitude shock compression experiments reported herein, pressure alone is not sufficient to produce amorphization, and localized effects due to shear play an important role. Shear strains cause inelastic lattice displacement above the elastic–plastic transition. In particular, the resolved shear stress on {111} planes leads to stacking-fault formation. Multiple high-resolution TEM observations indicate that the amorphous bands initiate in regions with stacking-fault concentration and preferentially when two different sets of {111} stacking-fault variants intersect. They start growing along directions that reasonably align with the predominant stacking-fault variant, not necessarily coincident with the plane of maximum shear. As they thicken, their orientation changes to that of maximum shear, which makes an angle of 10^0 with the former. MD simulations also indicate that a few ps after formation, the amorphous bands are still under uniaxial compression, which leads to a slight deviation from the equilibrium {111} lattice plane toward the maximum shear direction (approximately 10° away). The motion of dislocations also results in localized plastic work, which may be quite large for covalently bonded silicon. Furthermore, non-hydrostatic stresses can lower the melting temperature of materials under strong shock compression in addition to the reduction of melting temperature with pressure for silicon.

The pressure-induced diamond cubic to β-Sn and other phase transitions [30–34] are considered kinetically unfavorable in laser shock compression due to the rapid stress pulse decay, within nanoseconds. However, varying the

laser pulse conditions might lead to a phase transformation. As the laser energy increases, the amorphous bands can be observed deeper into the material due to the higher peak pressure/shear stress whereas the shock-generated heat is sufficient to nanocrystallize the layer close to the surface.

The observed amorphization is driven by rapid application of pressure and shear. Dynamic uniaxial loading produces large shear stresses that lower the threshold amorphization pressure as previously reported under conditions of static compression [6]. Fabrication of fully-dense amorphous and nanocrystalline silicon can be accomplished within extremely short timescales by appropriate choice of laser shock parameters, yielding a new method to design amorphous/nanocrystalline silicon micro/nano-electrical–mechanical-photonic systems [35].

Acknowledgments

This research is funded by a UC Research Laboratories Grant (09-LR-06-118456-MEYM) and a National Laser Users Facility (NLUF) Grant (PE-FG52-09NA-29043). We acknowledge the highly professional support of the LLE Omega laser facility and supporting staff in addition to Tane Remington for target assembly. Microscopy performed as part of a user proposal supported by Oak Ridge National Laboratory's Center for Nanophase Materials Sciences (CNMS), which is an Office of Science User Facility. We thank Dorothy Coffey for assistance with the FIB sample preparation. Computational resources supported by DOE Office of Science, Office of Advanced Scientific Computing (ASCR) via the Exascale Co-design Center for Materials in Extreme Environments. EMB thanks support from a ANCyT grant (PICT-0092) and a Secretaria de Ciencia Tecnica y Posgrado-U.N.Cuyo grant (2003-2015 M003).

Appendix A. Supplementary data

Supplementary material related to this article can be found online at http://dx.doi.org/10.1016/j.eml.2015.10.001.

References

[1] P.W. Bridgman, Phys. Rev. 48 (1935) 825.
[2] E. Teller, J. Chem. Phys. 36 (1962) 901.
[3] H.C. Chen, J.C. Lasalvia, V.F. Nesterenko, M.A. Meyers, Acta Mater. 46 (1998) 3033.
[4] V.I. Levitas, R. Ravelo, Proc. Natl. Acad. Sci. USA 109 (2012) 13204.
[5] A. Shah, P. Torres, R. Tscharner, N. Wyrsch, H. Kenner, Science 285 (1999) 692.
[6] S.K. Deb, M. Wilding, M. Somayazulu, P.F. McMillan, Nature 414 (2001) 528.
[7] A. Hedler, S.L. Klaumünzer, W. Wesch, Nature Mater. 3 (2004) 804.
[8] D. Clarke, M. Kroll, P. Kirchner, R. Cook, B. Hockey, Phys. Rev. Lett. 60 (1988) 2156.
[9] M. Gamero-Castaño, A. Torrents, L. Valdevit, J.-G. Zheng, Phys. Rev. Lett. 105 (2010) 145701.
[10] V.F. Nesterenko, Dynamics of Heterogeneous Materials, 1st, Springer-Verlag, 2001.
[11] Ch.E. Lekka, D.G. Papageorgiou, G.A. Evangelakis, J. Nanosci. Nanotechnol. 9 (2009) 4656.
[12] A. Loveridge-Smith, A. Allen, J. Belak, T. Boehly, A. Hauer, B. Holian, D. Kalantar, G. Kyrala, R. Lee, P. Lomdahl, M.A. Meyers, D. Paisley, S. Pollaine, B.A. Remington, D. Swift, S. Weber, J. Wark, Phys. Rev. Lett. 86 (2001) 2349.
[13] S.J. Turneaure, Y.M. Gupta, J. Appl. Phys. 111 (2012) 026101.
[14] S. Plimpton, J. Comput. Phys. 117 (1995) 1.
[15] E.M. Bringa, K. Rosolankova, R.E. Rudd, B.A. Remington, J.S. Wark, M. Duchaineau, D.H. Kalantar, J. Hawreliak, J. Belak, Nature Mater. 5 (2006) 805.
[16] T. Kumagai, S. Izumi, S. Hara, S. Sakai, Comput. Mater. Sci. 39 (2007) 457.
[17] J. Tersoff, Phys. Rev. B 38 (1988) 9902.
[18] P.K. Schelling, Comput. Mater. Sci. 44 (2008) 274.
[19] A. Stukowski, Modelling Simul. Mater. Sci. Eng. 18 (2010) 015012.
[20] L.M. Hale, D.-B. Zhang, X. Zhou, J.A. Zimmerman, N.R. Moody, T. Dumitrica, R. Ballarini, W.W. Gerberich, Comput. Mater. Sci. 54 (2012) 280.
[21] S. Phillpot, J. Lutsko, D. Wolf, S. Yip, Phys. Rev. B 40 (1989) 2831.
[22] J. Godet, L. Pizzagalli, S. Brochard, P. Beauchamp, Phys. Rev. B 70 (2004) 054109.
[23] L. Gómez, A. Dobry, C. Geuting, H. Diep, L. Burakovsky, Phys. Rev. Lett. 90 (2003) 095701.
[24] M.A. Meyers, Dynamic Behavior of Materials, John Wiley & Sons, 1994.
[25] L.V. Al'tshuler, Sov. Phys. Usp. 8 (1965) 52.
[26] S.J. Turneaure, Y.M. Gupta, Appl. Phys. Lett. 91 (2007) 201913.
[27] P.F. McMillan, M. Wilson, D. Daisenberger, D. Machon, Nature Mater. 4 (2005) 680.
[28] O. Mishima, L.D. Calvert, E. Whalley, Nature 310 (1984) 393.
[29] M.A. Hopcroft, W.D. Nix, T.W. Kenny, J. Microelectromech. Syst. 19 (2010) 229.
[30] A. Mujica, A. Rubio, A. Muñoz, R. Needs, Rev. Modern Phys. 75 (2003) 863.
[31] H. Kishimura, H. Matsumoto, N.N. Thadhani, J. Phys. Conf. Ser. 215 (2010) 012145.
[32] G. Mogni, A. Higginbotham, K. Gaál-Nagy, N. Park, J.S. Wark, Phys. Rev. B 89 (2014) 064104.
[33] K. Mizushima, S. Yip, E. Kaxiras, Phys. Rev. B 50 (1994) 14952.
[34] J.M.D. Lane, A.P. Thompson, T.J. Vogler, Phys. Rev. B 90 (2014) 134311.
[35] L. Pavesi, L. Dal Negro, C. Mazzoleni, G. Franzò, F. Priolo, Nature 408 (2000) 440.